HEBF strategy: a hybrid evidential belief function in geospatial data analysis for mineral potential mapping

Mahyadin Mohammadpour [a], Abbas Bahroudi [a, *], Maysam Abedi [a]

[a] *School of Mining Engineering, College of Engineering, University of Tehran, Iran.*

A B S T R A C T

In integrating geospatial datasets for mineral potential mapping (MPM), the uncertainty model of MPM can be inferred from the Dempster – Shafer rules of combination. In addition to generating the uncertainty model, evidential belief functions (EBFs) present the belief, plausibility, and disbelief of MPM, whereby four models can be simultaneously utilized to facilitate the interpretation of mineral favourability output. To investigate the functionality and applicability of the EBFs, we selected the Naysian porphyry copper district located on the Urmia – Dokhtar magmatic belt in the northeast of Isfahan city, central Iran. Multidisciplinary datasets- that are geochemical and geophysical data, ASTER satellite images, Quickbird, and ground survey- were designed in a geospatial database to run MPM. Implementing the Dempster law through the intersection (*And*) and union (*OR*) operators led to different MPM performances. To amplify the accuracy of the generated favourability maps, a combinatory EBFs technique was applied in three ways: (1) just *OR* operator, (2) just *And* operator, and (3) combination of *And* and *OR* operators. The plausibility map (as mineral favourability map) was compared to Cu productivity values derived from drilled boreholes, where the MPM accuracy of the hybrid method was higher than each operator. Of note, the success rate of the hybrid method validated by 21 boreholes was about 84%, and it demarcates high favourability zones occupying 0.67 km^2 of the studied area.

Keywords: *Hybrid method, Evidential Believe Functions (EBFs), Geospatial dataset, Porphyry copper, Naysian district.*

1. Introduction

The correct identification and exploration of mineral sources save human and financial resources. During the exploration of mineral reservoirs, geological, geochemical, geophysical, and drilling data are generated qualitatively and quantitatively on various scales with different techniques and accuracies. This reveals the necessity of developing MPM techniques in exploring mineral reservoirs in order to systematically manage various geospatial datasets. Developing such MPM algorithms falls under the umbrella term of spatial multi-criteria decision-making (SMCDM) issues, where experts utilize several geospatial criteria which are in close association with sought ore-forming targets [1].

To the best of our knowledge, the notion of MPM as a painstaking work was coined by Cargill and Clark in 1978 [2] who sparked development in geospatial data integration. There have been several studies dedicated to the use of geospatial data integration. MPM is typically generated by combining various evidential (or predictor) maps. These evidential layers are introduced and merged based on their spatial or genetic association with the target mineralization type. To make MPM a more effective exploration tool for huge amounts of disparate data sets at different scales, appropriate conceptual models with the existing mineralization type have been recommended. Improving the understanding of the processes that have a substantial impact on ore deposit formation is a tremendously important part of MPM, which helps geoscientists to reinforce their predictive capabilities. It is accessible through an Exploration Information System (EIS). The EIS implementation requires; 1) generating information from the data, 2) producing knowledge (using ore formation conditions or conceptual model), and 3) gaining insight into the development of target ore deposit strategies. Thus, executing three steps of converting data into information, information into knowledge, and knowledge into insight, assists the EIS to facilitate MPM and provide a platform for converting information into effective evidential maps related to the mineralization type of the area [3,4]. After the EIS preparation, it is necessary to combine the evidential layers with appropriate integration models. Five approaches have been proposed for spatial data integration [5], where among all, the data- and knowledge-driven ones are more popular. Every algorithm has pros and cons. Inevitably, pitfalls or drawbacks in the various strategies for MPM are not always laid bare, and there is a 'No thumb rule' or 'No free lunch' about which an algorithm is called the most suitable for MPM!

Hidden relationships between ore occurrences and evidential layers are searched within a set of training samples in the data-driven MPMs. Accordingly, several retrospective methods were successfully employed in regions with known locations of mineral occurrences [1]. Among popular techniques, weights of evidence [6], artificial neural network [7-9], support vector machine [10], and random forest [11] are often implemented. In knowledge-driven MPMs, the evidence is weighted based on the experts' judgment. Hence, these methods may add uncertainty to spatial data owing to the limitation in expert knowledge [12]. These methods include index overlay [13], fuzzy logic [14,15], fuzzy-AHP [16], and wildcat mapping [17]. Hybrid methods also integrate both the expert knowledge and location of known mineral occurrences. In fact, they are data-knowledge-driven methods [18-20].

Multiple data-driven methods are available which apply expert-based

* Corresponding author. Tel/Fax: +98-2182084551, *E-mail address:* bahroudi@ut.ac.ir (A. Bahroudi).

weights of geospatial evidential features through an experimental function. Furthermore, such methods are not based on training data [17,21]. For instance, logistic functions were applied in weighting spatial evidence in MPM [22-25]. Using a logical function to prepare evidence layers and produce powerful indicators in each region (greenfield or brownfield) is of central importance [24].

Due to the complex nature of terrains and the limitations on data extraction and exploration data, evidential layers are always suffering from uncertainty. Given the uncertainties in evidential maps, MPM also entails uncertainties. It can also be useful and effective to use an appropriate integration model which determines uncertainty in MPM. From 1970 to 1990, the emergence of smart systems indicated the rapid growth in the interest of artificial intelligence (AI) in issues related to uncertainty management and evidence reasoning. Dempster–Shafer (DS) evidence theory was developed based on belief function and reasoning independent of AI [26-28]. Out of the many approaches, this method seems to be robust for uncertainty management in smart systems. The evidence theory of the DS, based on evidence combination and data integration, attracted significant attention. Later, geoscience information was described for data integration on the basis of interpreting the DS rules. Meanwhile, An et al. (1994) managed or displayed uncertainty in explorative data integration using four EBFs, which include belief, disbelief, uncertainty, and plausibility functions [29]. The initial application of the EBFs in MPM was designed based on the experts' knowledge [29-31].

To run the DS model in MPM, two independent maps (i.e. belief and disbelief, or belief and uncertainty) are required to be estimated and allocated to each evidence layer [32]. Carranza and Hale (2003) introduced relevant equations for implementing the data-driven EBFs in MPM [33]. The data-based variant of the EBFs method was later developed and employed in landslide prediction [34], groundwater potential mapping [35], hydrocarbon resources potential mapping [36], and geothermal potential mapping [37].

In applying the EBFs method in MPM and its development, the values of two independent evidence classes, namely belief (Bel) and uncertainty (Unc) are assigned to each layer, and the plausibility (Pls) and disbelief (Dis) values are subsequently inferred. Upon generating these functions, the evidence layers are integrated based on the DS law, which is typically run by the intersection (*And*) and union (*OR*) operators [12]. In this research, we endeavored to follow very original work connected with MPM, where a novel EBFs strategy is profoundly explained. Since these operators have various functionalities, the generated belief maps are different. In the present study, to assess the performance of these operators, all evidential mappings were integrated once with *OR* operator, once with *And* operator, and finally with their combination (hybrid evidential belief functions "HEBFs"). It was observed that the combination form resulted in a better MPM in the Naysian porphyry copper district.

2. Materials and Methods

2.1. Hybrid Evidential Belief Functions

The EBFs theory was introduced from Dempster's work on generalizing the Bayesian inference, and lower and upper limits of probability [26,27]. Shafer (1976) presented the lower and upper limits according to the belief degree and the plausibility of belief functions theory [28]. When an SMCDM is designed, the concept or a set of all possible scenarios can be established for the proposed objectives as $\theta = [a_1, a_2, a_3, ..., a_n]$. Here, each proposition is defined by a subset of θ comprising those geological characteristics or environments that are the right objective. Function $m:2^\theta \to [0,1]$ is the basic probability measure, such that [29,33];

$$m(\varphi)=0 \tag{1}$$

and

$$\sum_{a \subset \theta} m(a) = 1 \tag{2}$$

Where, (a) is indeed a subset of θ. The quantity of $m(a)$ is a's basic

probability number, which is a measure of belief committed to (a). Taking these conditions into account means that no belief is attributed to an empty set ϕ and in addition the total belief takes value 1. The total belief is shown by H, as calculated by [29,33]:

$$Bel(H) = \sum_{a \subset H} m(a) \tag{3}$$

The plausibility function $Pls:2^\theta \to [0,1]$ is defined by the disbelief (Dis) function as following [29,33]:

$$Pls(H) = 1 - Dis(\text{H}) \tag{4}$$

Belief and plausibility concerning H, Bel(H), and Pls(H) are the lower and upper probabilities, respectively. Therefore, the degree of uncertainty regarding H is presented as below [29,33]:

$$\text{Unc(H)} = \text{Pls(H)} - \text{Bel(H)} \tag{5}$$

Once the degree of uncertainty is zero,

$$\text{Bel(H)}+\text{Dis(H)} = 1, \tag{6}$$

which is a Bayesian probability [29,33].

Assume that there is an explorative area ψ with a set of geospatial data sets X = [D$_1$, D$_2$, ..., D$_n$], where D$_i$ (i = 1, 2, ..., n) is a set of data or spatial data layer and includes the definite geophysical, geochemical or geological characteristics. Four pieces of evidence are separately prepared for each dataset or exploration layer: belief, disbelief, plausibility, and uncertainty. For instance, if the sought ore-forming target involves a massive sulfide deposit in a region of interest, certainly the areas of volcanic rocks in the geological map should be assigned a higher level of support (more weight), and subsequently a lower support level (less weight) for the barren rocks. The strong anomalies in earth's electromagnetic (EM) map (in association with geoelectrical properties) take stronger support (more weight), and a weaker one (less weight) for weak anomalies (barren areas) [29].

Knowledge-driven MPM is a fascinating technique for greenfield geologically areas where a lack of knowledge about mineral deposits exists. Belief functions are initially allocated to any evidential mapping based on the knowledge of the experts (as members of a decision-making team) in accordance with the sought mineral target in the ψ region. Noteworthy, no statistical analysis is conducted such that the values of absolute probability are not roughly needed, but two relative relationships must be determined accurately. The first one is the relative order of probabilities assigned to different attributes in a single data layer (scoring), D, and the second one is the relative order of probabilities among different geospatial layers [29].

To run the EBFs in MPM, the estimated belief functions can be integrated by the integrative role of the DS. Assume that there are two belief functions, namely Bel$_1$, represented by D$_1$ (or A), and Bel$_2$, represented by D$_2$ (or B). Using the integrative role of the DS as per the *OR* operator, the values of belief function probability are then calculated [29,32]:

$$Bel_C = \frac{Bel_A Bel_B + Bel_A Unc_B + Unc_A Bel_B}{\beta} \tag{7}$$

$$Dis_C = \frac{Dis_A Dis_B + Dis_A Unc_B + Unc_A Dis_B}{\beta} \tag{8}$$

$$Unc_C = \frac{Unc_A Unc_B}{\beta} \tag{9}$$

Relationships between the integrated evidential functions regarding the two spatial evidential layers (A and B) are defined in accordance with the *And* operator as [32,18]:

$$Bel_C = \frac{Bel_A Bel_B}{\beta} \tag{10}$$

$$Dis_C = \frac{Dis_A Dis_B}{\beta} \tag{11}$$

$$Unc_C = \frac{Unc_A Unc_B + Unc_A Bel_B + Unc_B Bel_A + Unc_A Dis_B + Unc_B Dis_A}{\beta} \tag{12}$$

where $\beta = 1 - Bel_A Dis_B - Bel_B Dis_A$ is a normalizing factor for approving Bel + Unc + Dis = 1.

Unlike most strategies in MPM, the EBFs refer to the ability to explicitly show the evidence uncertainty, even concerning the

unavailable evidence. In this method, two operators (*And* and *OR*) can be used to combine the layers, and a suitable operator can be used in different conditions. The only possible disadvantage is that two evidence class scores (belief and uncertainty) can be taken simultaneously into account. In this study, independent experts (six experts) were hired to reduce the error in specifying the values of the evidential belief functions for each layer. With four complementary output mappings, the EBFs provide more evaluation tools for analyzing the efficiency of the predictive models. Such modeling provides more layers of ground information which would be useful potentially in correctly leading the next explorative activities [18]. It is necessary to carry out comprehensive and systematic prospecting work through the EBFs.

2.2. Fractal Method

Most natural phenomena, particularly pertaining to earth sciences, are not in accordance with the regular dimensions of Euclidian geometry. For this reason, another geometry should be used to describe the events in nature in this connection. Mandelbrot (1983) was the first researcher who presents another geometry called fractal, based on which the processes in nature can be studied [38]. Cheng et al. (1994) were the first to use the concentration – area (C-A) fractal on the porphyry Cu-Au deposit of Mitchel-Sulphurests in Canada to classify the geochemical anomalies spatially [39]. Generally, geospatial data sets in mineral exploration have a multi-fractal behavior, highlighting the number of changes in geological, tectonic, geochemical, geophysical, and alteration conditions. These behaviors are mostly controlled by the enrichment and deposit formation stages. By confirming these characteristics with geospatial data, the modeling works perfectly (such as [40-42]). The C-A multifractal model is based on the area occupied by each special concentration in the studied region and presented by a series of simple experimental equations [39]. This experimental model expresses that the area ($A(\rho)$), enclosed with the values of concentration (ρ), less than a pre-determined threshold (υ), followed the following exponential relation [39]:

$$A(\rho \leq \vartheta) \propto \rho^{-\alpha} \qquad (13)$$

where, $A(\rho)$ is the occupied area with a concentration beyond the alignment curve ρ; υ is the threshold, and α is the fractal dimension [39].

3. Geological setting and Geospatial data set

The studied area is the Naysian Porphyry Cu-Mo District (NPCMD) located on eastern longitudes 52°26' to 52°29' and northern latitude 32°54' to 32°56' in northeastern Isfahan. It covers an area of about 6 km² (Figure 1a). According to the Stocklin divisions (1968) [43], the Naysian district covers a part of the Urmia-Dokhtar Magmatic Assemblage (UDMA) belt [43,44]. Having the form of a volcanic strip, this belt is located W-SW of the central Iran domain and the N of the Sanandaj-Sirjan zone (SSZ). This strip is composed of volcanic and volcano-sedimentary series with a general trend along the NW-SE of the country. The UDMA is comprised of volcanic and intrusive masses from the Eocene to the quaternary with 1700, 50, and 4 km in length, width, and thickness, respectively [45]. This belt overlaps with the global metalorganic and orogeny belt of Alpine – Himalayas. Moreover, similar to other magmatic arcs on the continental margin such as Andes and Cordillera, it hosts most of the Cu-Mo deposits in Iran together with other deposits pertaining to these geodynamic origins [46].

The NPCMD system has been investigated in numerous studies (e.g. [47-49]). The rocks in the NPCMD are categorized into volcanic – volcanoclastic and intrusive – sub-volcanic groups. From petrological points of view, volcanic rocks are often dacite, andesite, basaltic andesite, and basalt. Note that the intrusive rocks have a composition of granodiorite and tonalite stones. Magma content comprises sub-alkaline and calco-alkaline types. Naysian area is severely tectonized and dynamic. Long faults with an obvious trend of N55E, along with their intense interaction with the perpendicular faults of the UDMA

zone have a substantial impact on emplacing the stocks and expanding the alteration processes in the rocks. The main magmatic dikes have been injected in this region with an elongation of NE-SW trend. The alteration processes are drastic on the NPCMD, which are propylitic, phyllic, potassic, quartz–tourmaline, silica, and FeO zones, respectively larger [50]. Figure 1b presents an enlarged view of the geological map, with a scale of 1:1000.
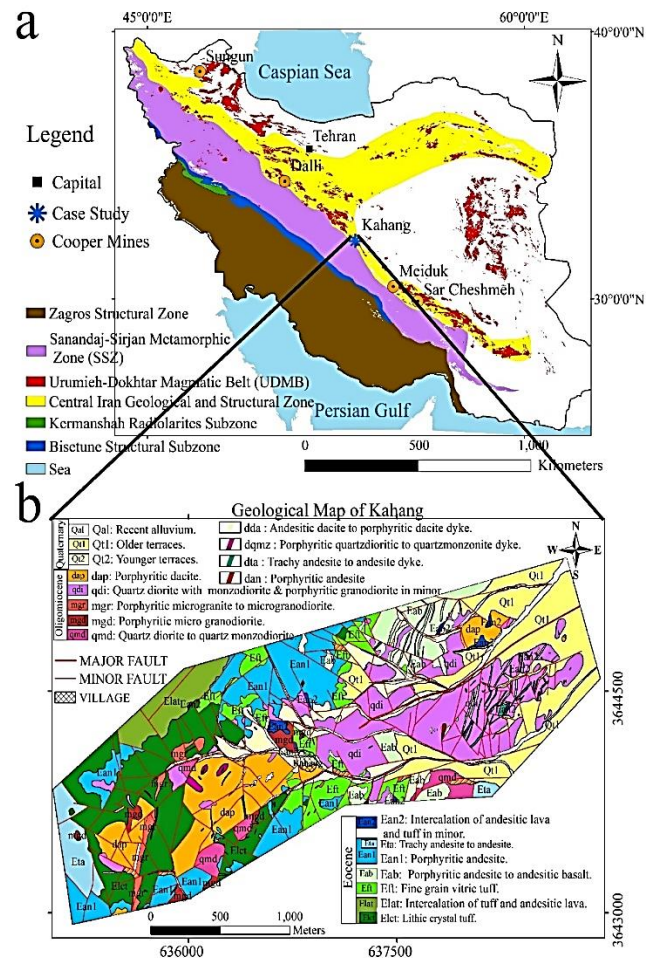

Figure 1. Geology and status of the explorative district of Naysian, (a) location of the Naysian district in the geological map of Iran, and (b) the detailed geological map of the Naysian district with a scale of 1:1000.

Based on geological evidence, the NPCMD was formed on the continental margin subduction zone of Arabian and Central Iran plates [43]. Porphyry Cu deposits along with monzonite and calco-alkaline granodiorite rocks were discovered on the tectonic belts of the continental margin subduction zone. Semi-deep intrusive masses mostly form stock. They sometimes form dike but rarely batholith. Calco-alkaline magma generated from the melting of a part of the ocean crust subduction zone escapes upside and creates chemical and mineralogical changes in the zone's rocks, thereby forming. Therefore, alteration and geochemical zonings are formed. In porphyry-type systems, the most important alterations from the center of ore deposition, are potassic, phyllic, argillic, and propylitic. Geochemical zoning reveals anomalous patterns of Ag, Mo, Cu, Pb, and Zn elements, respectively [51-53]. These rocks and alterations subsequently generate anomalous geophysical responses, where the magnetometry and electrical resistivity surveys are the most commonly applied methods [54,55]. Accordingly, in exploring the porphyry copper deposits, it is necessary to take into account the rock units, region's tectonic, alterations and chemical distribution of elements, and distinctive geophysical anomalies.

3.1. Geology Layers

The magmatic activity in the NPCMD is based on the Eocene rule and a series of lava-explosive eruptions combined with lithic tuffs and sometimes large-sized crystals [50]. In what follows, several pieces of evidence related to volcanic units are gradually seen among the aforementioned layers which are covered by the relatively high thickness of small-sized vitric tuffs. In the middle part of Eocene, lava eruption is detected with a variable change from andesite – andesite basalt to andesite – dacite and trachyte andesite. During Oligo-Miocene, intrusion, and placement of intrusive sub-volcanic units with a combination of quartz diorite, micro-granite, and porphyry dacite are observed. In the last stage and the youngest phase, which coincides with the placement of andesite dikes, dacite and quartz diorite have been yielded [50].

To apply the EBFs to Cu potential mapping in the Naysian region, the lithology layer was classified into nine classes. Intrusive rock controlling ore formation is the quartz diorite, occupying more than 70% of the main mass. Quartz diorite rocks often have a distinct porphyry texture, which gradually ends in granodiorite as quartz increases and phenocrysts become granular. Mineralization in the region includes the mineralized shear zones, specified by the host rock of porphyry quartz diorite, porphyry granodiorite, and in certain cases, shear dacite [50]. Therefore, the most belief scores are assigned to these rocks (Table 1). Through scoring the functions, as per Table 1, maps of four functions, namely belief, disbelief, uncertainty, and plausibility, were prepared for the lithology (rock types) layer. Figure 2 presents two independent maps of the Bel and Unc for rock types indicator.

To extract the alteration zones, satellite image processing was used as the initial processing step, and a field survey was then run to confirm the satellite processing result. Over the recent years, the application of remote sensing has been widely expanded in discovering various mineral resources (such as [56,57]). The most important feature of mineral exploration is that it identifies the alteration zones [58]. Since the alteration is directly related to the mineral resources and mineralization, their detection through satellite images has accelerated the exploration task and significantly reduced its operation cost.

Figure 2. Independent evidential maps obtained from rock type layer, (a) Belief map, and (b) Uncertainty map.

In the Naysian district, alteration zones have been extended, with the most frequent ones being potassic, phyllic, argillic, and propylitic [50]. In the present study, nine bands (VNIR, SWIR) of ASTER sensors were utilized to determine the alteration zones. The geometrical and radiometric corrections were performed on the images. To reveal the alteration zones on the images of the ASTER data, band ratio (BR) [59], selective principal component analysis (SPCA) [60], Least Squares Fit (LS-Fit) [61], and spectral angle mapper (SAM) [62] techniques were utilized. We forgo a full discussion of the details. Minerals with Al-OH like kaolinite, illite, pyrophyllite, and alunite, found in phyllic and argillic alterations were identified by ASTER image processing. Based on the geology of the region, examined maps, and obtained results, BR, SPCA, and LS-Fit techniques were used to determine the phyllic, argillic and propylitic zones, respectively. The initial result of remote sensing data analyses is shown in Fig. 3a.

The results of these examinations were in good agreement with the findings of field surveys, microscopic thin-sections, and XRD analysis [50]. Figure 3b presents the final alteration map derived from the field survey and satellite image processing. From the conceptual model of porphyry deposits, the highest score was assigned to the potassic alteration. Details on how to evaluate the alterations can be seen in Table 2. Four-evidence mappings were generated and the belief (Fig. 4c) and uncertainty (Fig.4d) outputs were plotted as independent maps.

Determining structural lineaments assist in the identification of the copper mineralization place. Here, structural lineaments were extracted from the geological map, satellite images, and geomagnetic signals. Then, a lineament density map was prepared. Figure 4a indicates the fault traces observed in the geological field survey. A suitable approach to capture the trace of the lineaments is from satellite images [63]. Visual picking of lineaments from the satellite images is the most common method, but it is a tough and time-consuming task. Hence, automatic techniques of lineament extraction can significantly reduce user error and implementation time. Where the most powerful and useable automatic extraction techniques are hybrid strategies for edge detection accompanied by line extraction [64-66]. In this research, a Canny algorithm [67] was employed as an edge detector filter, and then a Hough transform [68] was executed to extract the linear spatial features. The Canny algorithm has quite a performance in comparison with other edge detectors for the sake of dual-threshold selection and the maximum local gradient calculation [69,70]. Through automatic extraction of lineaments, the Hough transform does not take into account the gap between the lines, allowing for correct identification of the fault and contact traces [71,72]. These techniques here processed the images of the Quickbird satellite at a spatial resolution of 0.61 m with a Pan sensor, and 2.44 m with an MS sensor. Furthermore, it is currently among the most powerful commercial satellite images in terms of ground resolution. The Panchromatic band image was selected because we can detect the linear spatial features as an important indicator in close association with the ore mineralization systems. After satellite image corrections, the Canny filter detected the edges in the line extraction phase; afterward, the Hough transform could succeed in the post-processing phase to enhance the tectonic lineaments [73]. The lineament map related to the copper mineralization plots in Fig. 4b, where a prominent direction can be observed along the NE-SW.

Another method for plotting shallow and deep-seated lineaments is from geomagnetic data, so-called "geophysical lineaments" [74]. The ground-based magnetometry survey was conducted over a 5.2 km² area with a grid spacing of 20×50 m, where 4446 stations were measured with a proton magnetometer. Following diurnal correction, the regional magnetic trace was removed from the observations through a polynomial fitting approach. Different algorithms have been developed for lineament extraction in geophysics, most of which are constructed on the basis of the directional derivatives of the potential field magnetometry data. The present research made use of the tilt angle method, relying on the initial concepts of the horizontal and vertical derivatives of the total field magnetic data [75]. Prior to implementing the tilt angle filter, the reduced-to-pole (RTP) filter was applied to the
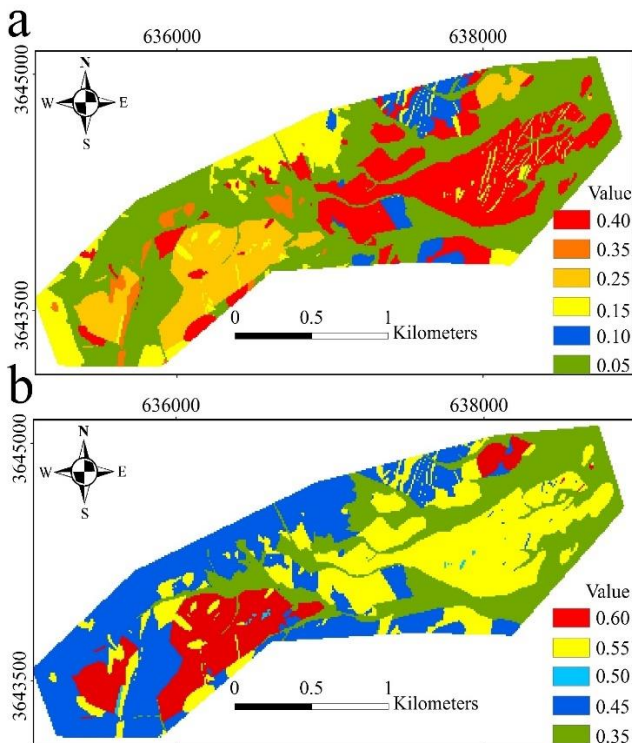
residual magnetometry data to amplify the amplitude of the signal and correct the effect of the earth's magnetic field inclination. It puts the positive portion of signals over the causative source(s) responsible for the magnetic anomaly. Figure 4c shows the output of the tilt angle method on the RTP data in the NPCMD, where zero values are located in the shallow or deep-seated lineaments.

Table 1: Values of Bel, Unc, Pls, and Dis for different rock types.

Class Units	Belief	Uncertainty	Plausibility	Disbelieve
QDI: Quartz diorite with monzodiorite	0.4	0.55	0.95	0.05
MGD: Porphyritic Micro granodiorite	0.35	0.55	0.9	0.1
DAC: Porphyritic dacite	0.25	0.6	0.85	0.15
Dyke	0.15	0.55	0.7	0.3
Silica vein	0.15	0.5	0.65	0.35
TAN: Trachy andesite to andesite	0.15	0.45	0.6	0.4
BAN: Porphyritic andesite to andesitic basalt	0.1	0.45	0.55	0.45
TUF: Intercalation of tuff and andesitic lava	0.05	0.45	0.5	0.5
QTA: Recent alluvium	0.05	0.35	0.4	0.6

The final lineament map was generated by merging all extractions from the geology map (field survey), Quickbird image, and the magnetometry data (Figure 4d). To generate the lineament indicator map, the lineament density map must be classified. For this purpose, we used the fractal geometry concept, which typically functions well [76,20].

To implement the C-A fractal method on the lineament density map [76,20], the intensity rather than the concentration of lineament density was taken into account. As shown in Figure 5a, a fractal curve was divided into four classes to introduce the Bel and the Unc maps. Each class was then weighted based on experts' attitudes summarized in Table 3. Regarding the connection of the lineaments (as the passing points of hydrothermal fluid circulation) and Cu-Mo mineralization, the highest value was assigned to the denser portions. Next, four evidential maps, namely Bel (Figure 5b), Pls, Unc (Figure 5c), and Dis were generated.

3.2. Geochemical Layers

The NPCMD was studied geochemically. In view of the wide soil coverage in the region and the implementation of exploration operations on a scale of 1: 5000, soil samples were harvested as the most appropriate geochemical method at this stage. With regards to the approximate trend of the mineralization and experiences obtained from the previous studies, the total azimuth of sampling was 134^0 and systematic sampling was conducted in the rectangle regular system. The sampling distance was related to a grid of 50 × 25 m, where the rectangular length was orthogonal to the probable mineralization trend (Figure 6a). The soil sampling size was considered between 40 and 60 mesh whereas 2564 samples were collected and analyzed by the ICP-OES equipment [77].

Results of concentration analyses showed that the main parageneses were Cu, Mo, and W elements, but the W quantity is very low. Therefore, Cu and Mo were considered geochemical indicators. Results of geochemical anomalies properly overlapped with the geological setting in the NPCMD. There are two types of mineralization here; one complying with the shear dacite stock or phyllic alteration, and another with the weak potassic alteration observed over the porphyry granodiorite unit [76]. Hence, the mineralization is likely controlled by

the porphyry quartz diorite and granodiorite units, where a low concentration of Cu together with the quantities of Mo were observed. Concerning the deposit characteristics in the region, geochemical indicator layers of Cu and Mo were selected in the MPM.
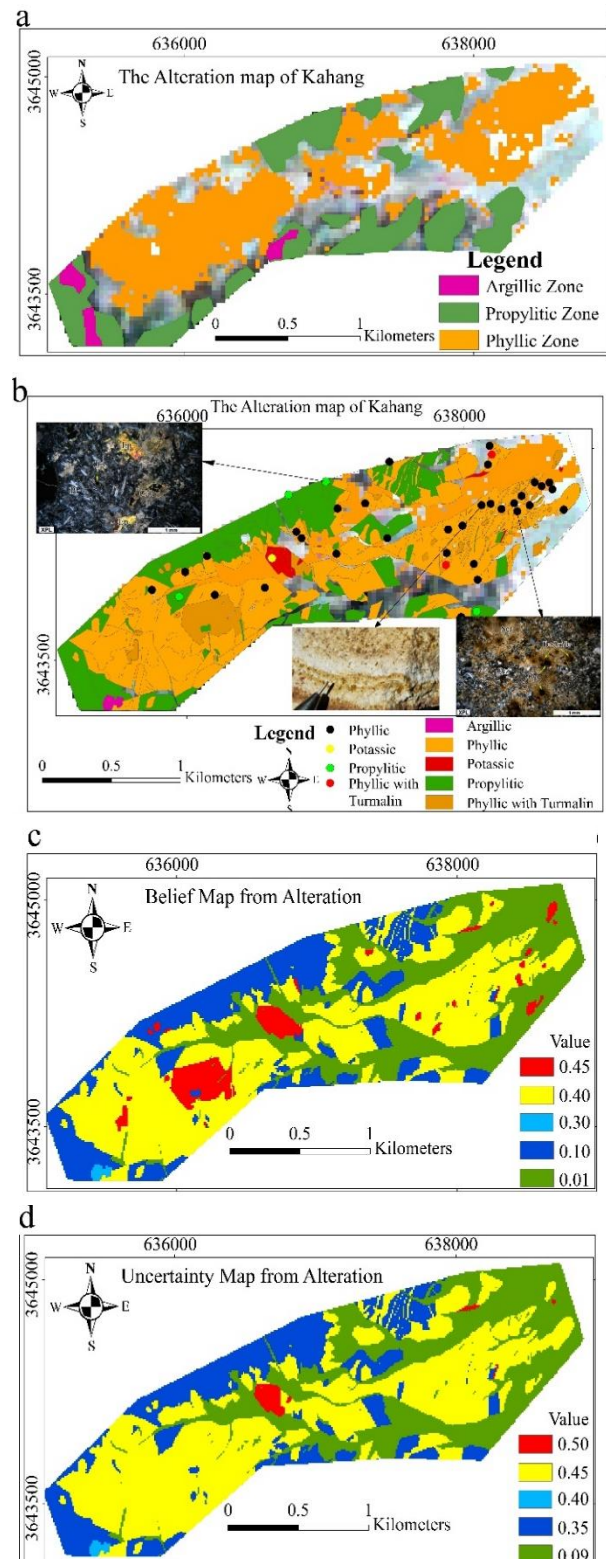

Figure 3. Alteration indicators in Naysian area, (a) alteration regions using ASTER images, (b) final alteration map after merging the field survey and remote sensing results, (c) belief map, and (d) uncertainty map.

Table 2: Values of Bel, Unc, Pls and Dis for different alterations.

Class Alteration	Belief	Uncertainty	Plausibility	Disbelief
Potassic	0.45	0.5	0.95	0.05
Phyllic with turmalin	0.45	0.45	0.9	0.1
Phyllic	0.4	0.45	0.85	0.15
Argillic	0.3	0.4	0.7	0.3
Propylitic	0.1	0.35	0.45	0.55
Others	0.01	0.09	0.1	0.9
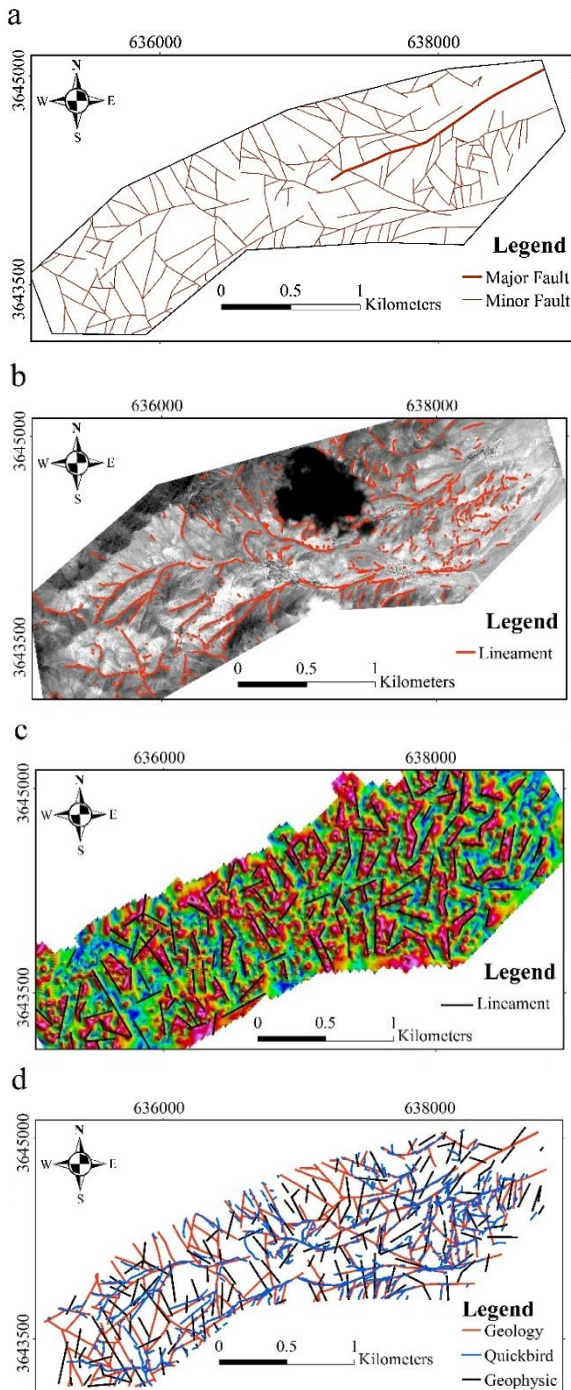
Figure 4. The structural lineaments in the Naysian region were extracted from (a) field survey, (b) Quickbird satellite image processing, (c) the tilt angle mapping of the ground-based magnetometry survey, and (d) final lineament map via integrating all the maps.

After correcting the censored values and outliers, the C-A multifractal method was used for separating the anomalous regions from the background. Figures 6b and 7a show the fractal curves of the Cu and Mo elements, respectively. Element distribution maps were also reclassified and assigned scores. The inverse distance weighted (IDW) technique was utilized to interpolate the geochemical data [78]. The highest belief value was allocated to the regions with anomalous concentrations of Cu and Mo in association with the porphyry-type ore mineralization. Tables 4 and 5 show how these scores were assigned to each class derived from the fractal curve, for Cu and Mo, respectively. Finally, Bel and Unc maps were generated in Figure 6c, 6d for Cu element and Figsure 7b and 7c for Mo

3.3. Geophysical Layer

Various techniques have been dedicated to edge detection of the potential field magnetometry data, the use of directional gradients, downward continuation, and several high-pass filters. Out of them, an analytic signal (AS) is a filter that is conducive to enhancing the borders and main body of the sought targets [79-81]. This filter approximately captures the borders of the magmatic intrusive-related sources in cases of generating an intense magnetic signature. The analytic signal map was implemented on the RTP magnetometry data (Figure 8a) and then was classified after applying the C-A multifractal method (Figure 8b). Fractal patterns become possible when the data distribution pattern shows the self-similarity and independence of the scale [82]. Owing to the self-similarity of geophysical data, they can also follow fractal patterns and it is possible to identify and separate geophysical anomalies using fractal geometry [83,84]. Since Cu-Mo mineralization occurred mostly on the margins of causative sources, those promising regions were closely related to the medium values of this filter. Based on the scores assigned in Table 6, the Bel (Figure 8c) and Unc maps (Figure 8d) were generated.

4. Results and Discussion

The EBFs have been used by geoscientists to model and integrate geospatial data to delineate the favorable regions associated with ore mineralization (e.g. [18,32]). Modeling through the EBFs displays the spatial data using uncertainty maps, which is an evident superiority over other modeling techniques in MPM. With two or more indicator maps, various logical operators can be used individually or simultaneously for data integration. In the EBFs model, *OR* and *And* operators, introduced by Ann et al. (1994a), are common to integrate the indicators for MPM [18,29].

The *OR* operator uses Eqs. 7,8 and 9 to integrate the evidential layers, where the outputs are controlled by the maximum value of inputs (corresponding to the risk-taking approach), and the integrated value in a location is only controlled by the most appropriate evidential maps. This operator is used in cases where the factors are low and the presence of each positive factor can be enough for utility expression [18]. The *And* operator uses Eqs. 10, 11, and 12 to integrate the evidential layers. The influence of this operator is that the output map is controlled by the lowest weight of layers in each status (corresponding to the risk-aversion approach), leading to a conservative estimation of the final prospectivity map. The *And* operator is suitable when there are two or more required pieces of evidence to confirm an event.

In practice, it is possibly appropriate to use a wide range of operators to amplify the accuracy of MPM. For instance, assume that two input maps reveal evidence of which is better to be connected. In this study, it is highly possible that mineralization occurred in the regions with both phyllic alteration and quartz diorite rocks. However, it is probable that in certain parts of the region, there are non-altered quartz diorite rocks, a phenomenon reducing the odds of ore mineralization. In such cases, *And* operator is appropriate for integration because, in each situation, integration is controlled by both explorative layers. In other cases, *OR* operator is more appropriate. Instead of integrating all indicators with a special operator such as *OR* or *And*, it might be better to use the operator suitable in each stage of the map integration process about the

factors of mineralization and their impacts on each other. This means that a hybrid operation "HEBFs" should be run to generate the final MPM by utilizing both *OR* and *And* operators. The decision tree shown in Figure 9 was used to implement the HEBFs algorithm.
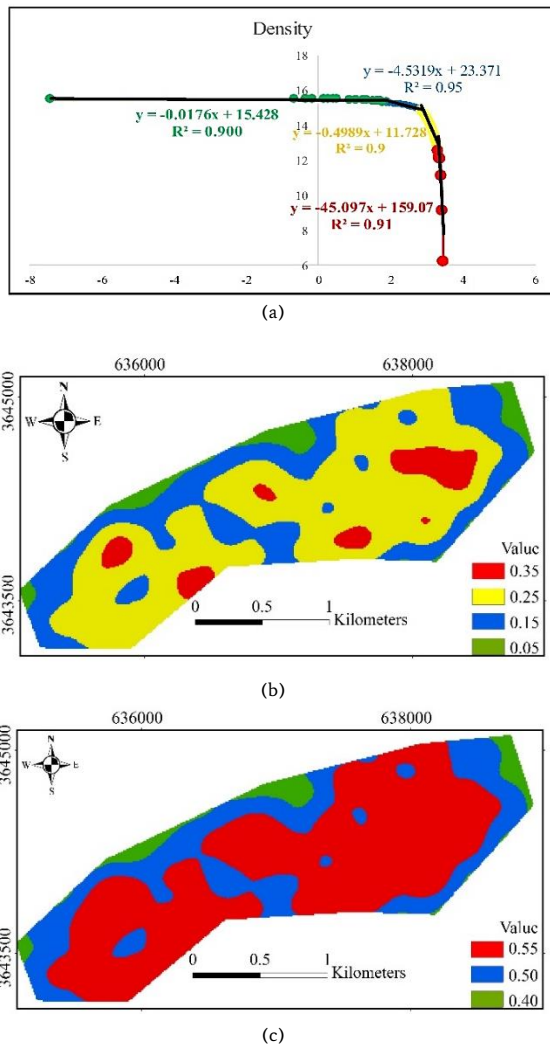

(a)

(b)

(c)

Figure 5. Evidential maps of lineament density, (a) the C-A multifractal curve, (b) belief map, and (c) uncertainty map.

Table 3. Values of Bel, Unc, Pls and Dis for four classes of fault density map.

Class Density	Belief	Uncertainty	Plausibility	Disbelief
D > 27.6	0.35	0.55	0.90	0.10
17.01 < D < 27.6	0.25	0.55	0.80	0.20
7.18 < D < 17.01	0.15	0.5	0.65	0.35
D < 7.18	0.05	0.40	0.45	0.55

Table 4. Values of Bel, Unc, Pls and Dis for geochemical Cu concentration.

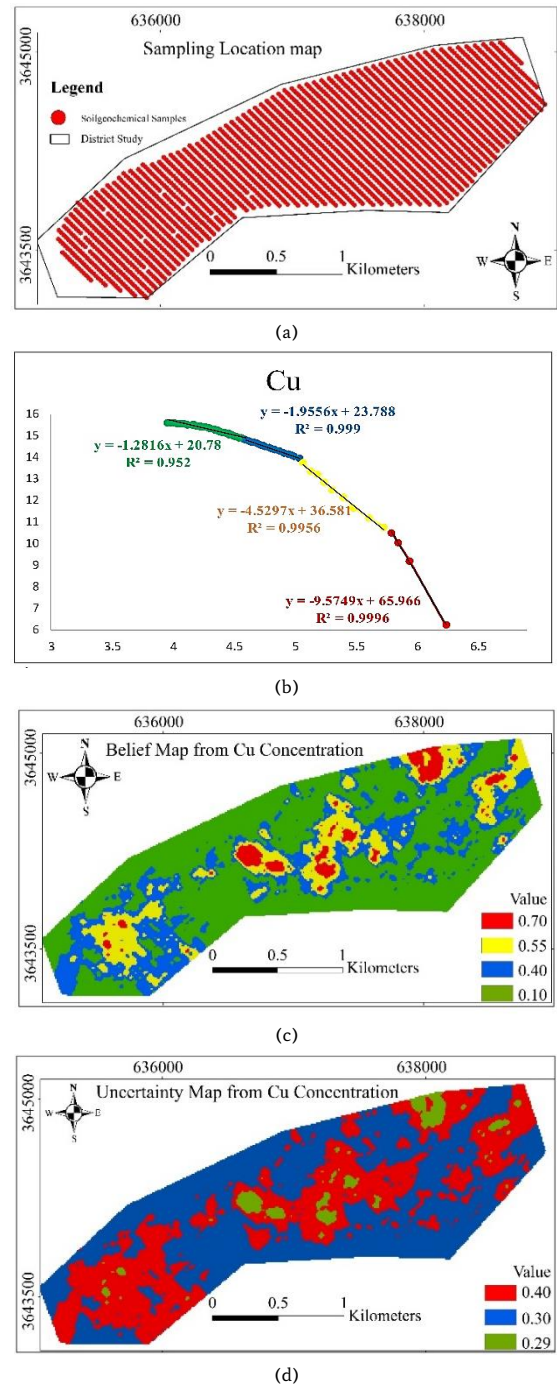| Class Concentration	Belief	Uncertainty	Plausibility	Disbelief
Cu > 306.88	0.7	0.29	0.99	0.01
153.17 < Cu < 306.88	0.55	0.4	0.95	0.05
99.7 < Cu < 153.17	0.4	0.4	0.8	0.2
Cu < 99.7	0.1	0.3	0.4	0.6

(a)

(b)

(c)

(d)

Figure 6. Copper geochemical evidential maps, (a) the location map of the soil geochemical samples in the region, (b) C-A multifractal curve, (c) belief map, and (d) uncertainty map.

Table 5. Values of Bel, Unc, Pls and Dis for geochemical Mo concentration.

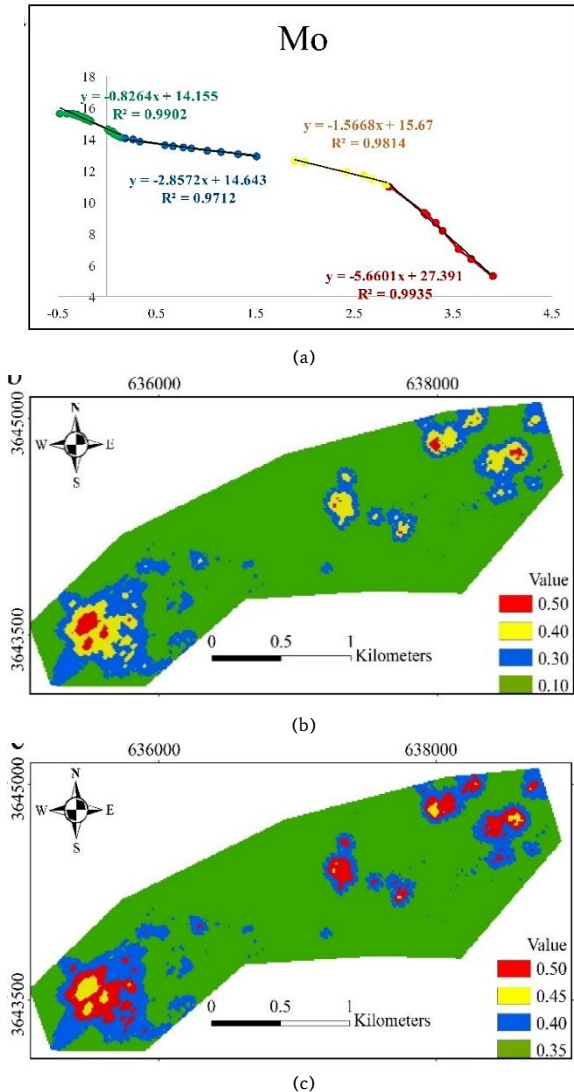| Class Concentration	Belief	Uncertainty	Plausibility	Disbelief
Mo > 16.94	0.5	0.45	0.95	0.05
4.5 < Mo < 16.94	0.4	0.5	0.9	0.1
1.15 < Mo < 4.5	0.3	0.4	0.7	0.3
Mo < 1.15	0.1	0.35	0.45	0.55

(a)

(b)

(c)

Figure 7. Molybdenum geochemical evidential maps, (a) C-A multifractal curve, (b) belief map, and (c) uncertainty map.

Table 6. Values of Bel, Unc, Pls and Dis for geophysics layer.

Class Value	Belief	Uncertainty	Plausibility	Disbelief
AS > 24.1	0.25	0.55	0.80	0.15
10.5 < AS < 24.1	0.30	0.6	0.90	0.10
4.08 < AS < 10.5	0.2	0.55	0.75	0.25
AS < 4.08	0.2	0.4	0.6	0.4

Here, three strategies were examined to integrate indicators in MPM generation. All layers were initially integrated by the *OR* operator (Figure 10), then, by *And* operator (Figute 11), and finally by the HEBFs (Figure 12). This inferential network (Figure 9) was designed in two stages according to the available exploration layers in the porphyry-type ore mineralization systems and expert opinion. In the first stage, the sub-layers were combined, and in the second stage, the main layers were combined. As shown in Figure 9, the main layers comprised geochemistry, geophysics, and geology. The sub-layers of geochemistry were Cu and Mo layers; the sub-layers of geology included rock type, alteration, and lineament density; and the sub-layers of geophysics consisted of the analytical signal layer.

The EBFs were applied on layers using *OR* operator and four maps were obtained. The belief map in Figure 10a shows that regions with high severity values were those with mineralization whereas no anomaly

evidence was detected in regions with low severity values. Figure 10b illustrates the uncertainty map. The map shows the uncertainty changes ranged from 0.0009 to 0.042 due to the use of the *OR* operator. Figure 10c shows the plausibility values in the study area that high severity values show the mineral favourability zones. Figure 10d shows the disbelief, in which the regions with high severity values indicate areas with lower mineralization evidence.
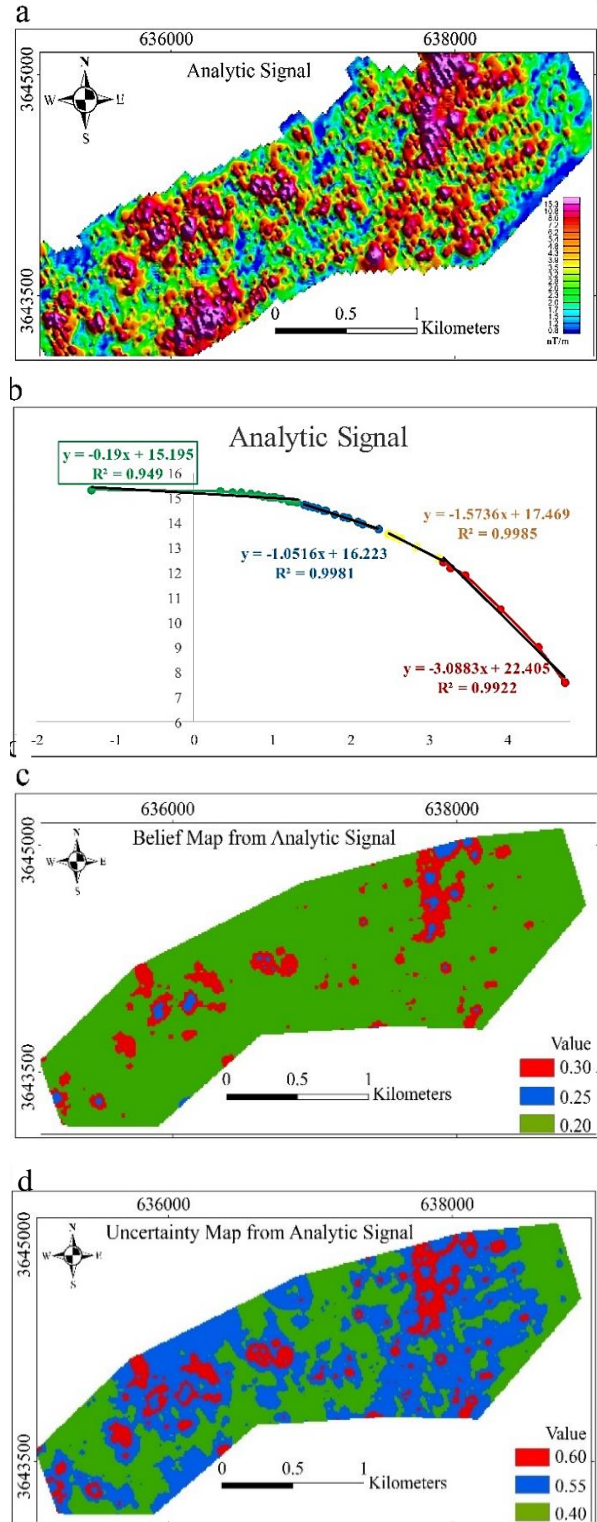

a

b

c

d

Figure 8. Geophysical evidential maps of the magnetometry analytic signal indicator, (a) analytic signal map, (b) C-A multifractal curve, (c) belief map, and (d) uncertainty map.
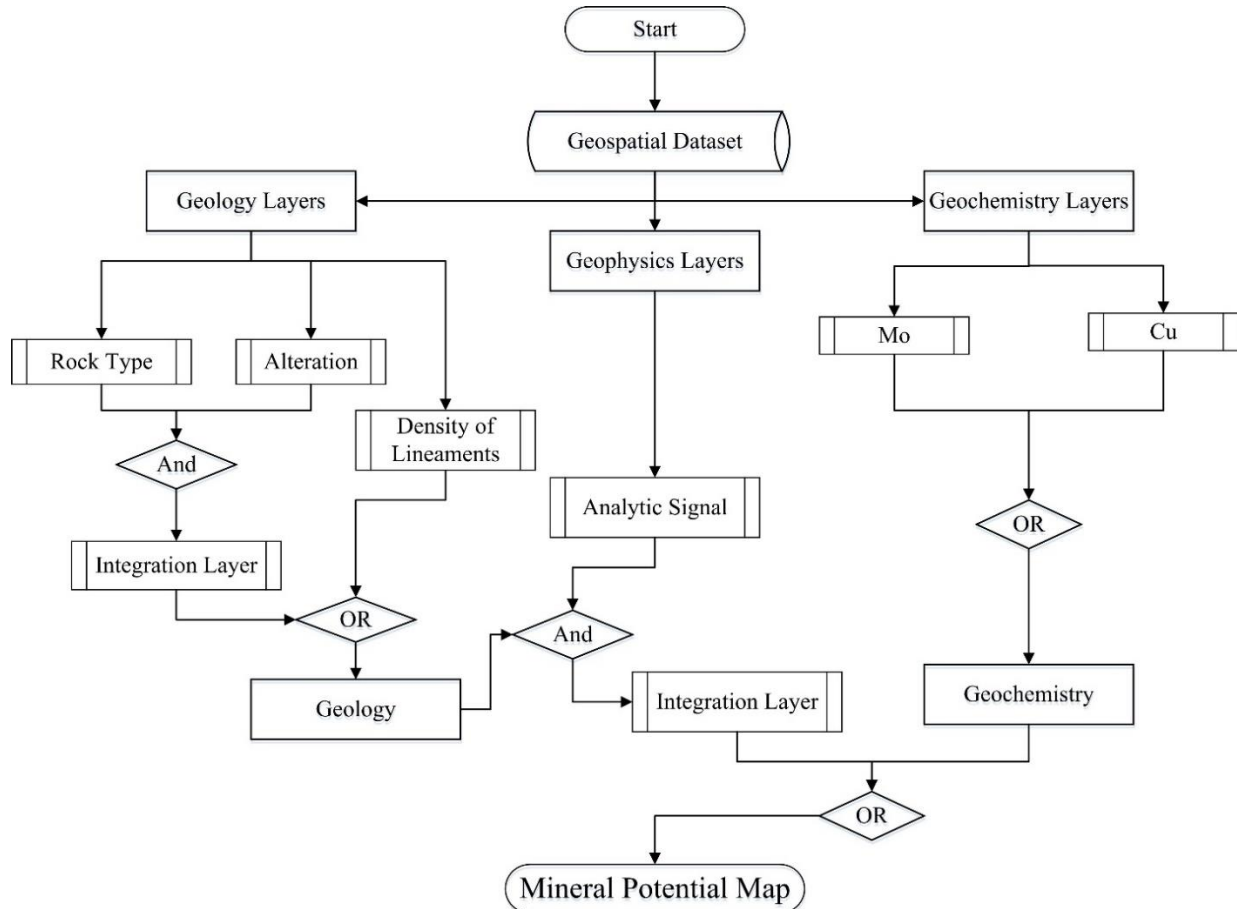
Figure 9. Decision-making tree designed for amplifying MPM through the hybrid EBFs technique.

The EBFs were applied based on the decision-making chart (Figure 9) using *And* operator. As seen in Figure 11, the application of *And* operator led to low values in the belief map (Figure 11a) and high values in uncertainty (Figure 11b), which was not suitable. Therefore, in the whole study area, the values of the plausibility map (Figure 11c) were close to 1 and the disbelief map values (Figure 11d) were close to zero. The HEBFs were applied based on the decision-making chart (Figure 9) using *And* and *OR* operators. The belief map (Figure 12a) clearly shows the regions with high mineralization possibility and the belief range was acceptable. Besides, the maximum belief value was 0.668. In the uncertainty map (Figure 12b), the value was between 0.137 and 0.773, which is a better result compared to the other two methods, indicating the uncertainty considering the exploratory evidence. The plausibility map (Figure 12c) in regions with high severity values introduces the mineral favorability zones. The disbelief map (Figure 12d) shows the areas with minimum mineralization evidence.

Within the studied region, 40 boreholes were drilled to evaluate the mining tonnage of the NPCMD. The Cu concentration was analyzed through atomic absorption equipment. To validate the results of MPM, the maximum Cu concentration along each borehole was considered. Once the maximum Cu concentration was calculated in each borehole, its value was compared to that of the plausibility map generated by the three aforementioned strategies. In Figure 13, the horizontal axis of the plots represents the logarithmic grade of Cu (due to the distribution of the lognormal Cu), and the vertical one indicates the plausibility value in pixel of borehole locations. Figures 13a, b and c were derived from *OR*, *And*, and the HEBFs strategies, respectively. It is obvious that higher Cu concentrations are positively correlated with higher values of plausibility in the MPM. Therefore, the closeness of the fitted linear curve (between the plausibility versus the Cu concentration) to a line with a slope of 45 degrees, indicates the higher accuracy of the

plausibility map. As observed in Figure 13, the slopes of all fitted lines are positive indicating the efficiency of the EBFs technique in MPM, meanwhile, those related to the HEBFs method were more than *OR* and *And* operators. In addition to the visualization interpretation, the correlation coefficient between Cu and the plausibility values in the location of boreholes was calculated by the Spearman method (Table 7). The correlation coefficient of Cu with the plausibility value in all three strategies was more than 0.7, indicating that MPM results were in good agreement with the reality. The correlation coefficient in the HEBFs method was higher than in the other two methods, indicating that the combination of both *OR* and *And* operators provided more optimal results.

To investigate the success rate of each strategy, the plausibility values were extracted from the drilling, where 25 out of 40 boreholes showed the maximum Cu concentration exceeding 0.5%. In this study, due to the plausibility values of the three methods, a 0.9 threshold was used to separate the anomaly zones. The thresholds obtained from data distribution were used for generating reclassified binary plausibility maps in Figure 14. In *OR* plausibility binary map (Figure 14a), seven boreholes (28%) were located within the mineral favourability regions with an area of 0.41 km². In *And* plausibility binary map (Figure 14b), 20 boreholes (80%) were located within the favorable regions occupying an area of 2.52 km². Although this map covered more boreholes, introduced much more area compared with the *OR* operator and confirmed its superiority over the *OR* map. In the HEBFs plausibility map (Figure 14c), 21 (84%) boreholes were located within the favorable zones covering an area of 0.67 km². Hence, it indicates the most successful drilled boreholes by capturing less area compared with *And* operator. This shows the higher efficiency of the hybrid form in MPM through implementing the EBFs. Note that the SW portions of the NPCMD seem very promising for further exploration and drilling.
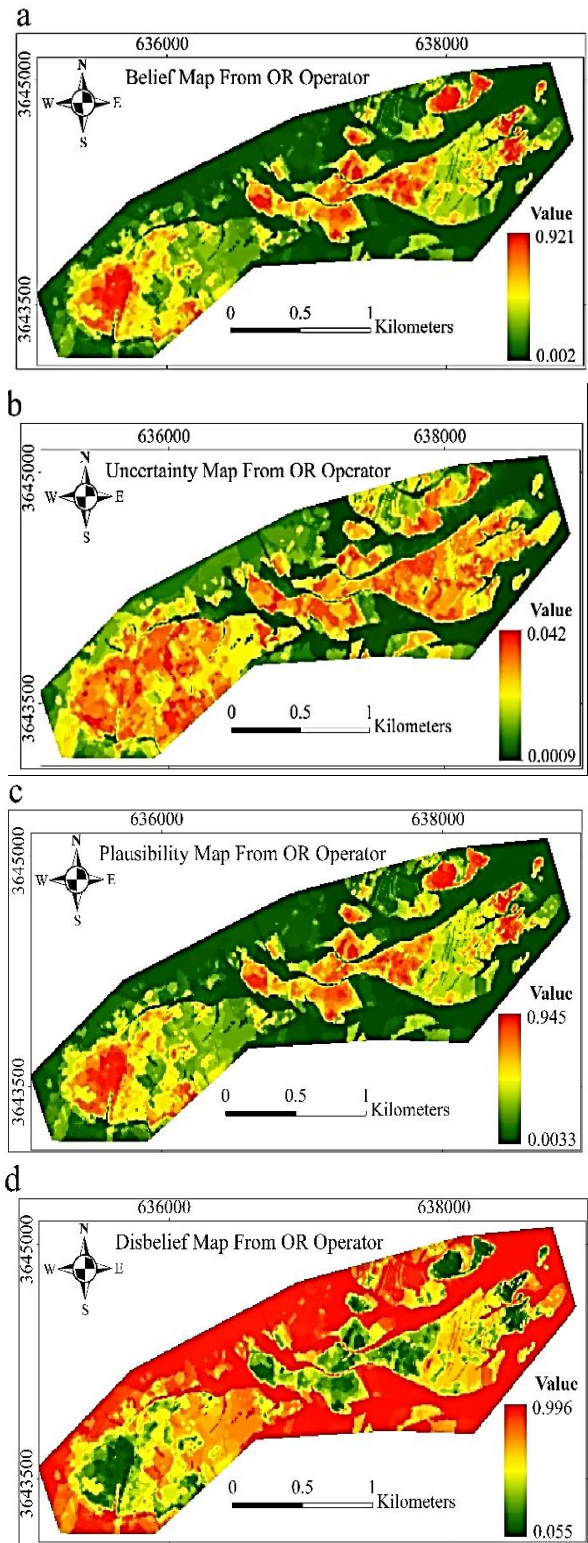
Figure 10. Maps obtained from the EBFs model using the OR operator, (a) belief map, (b) uncertainty map, (c) plausibility map, and (d) disbelief map.
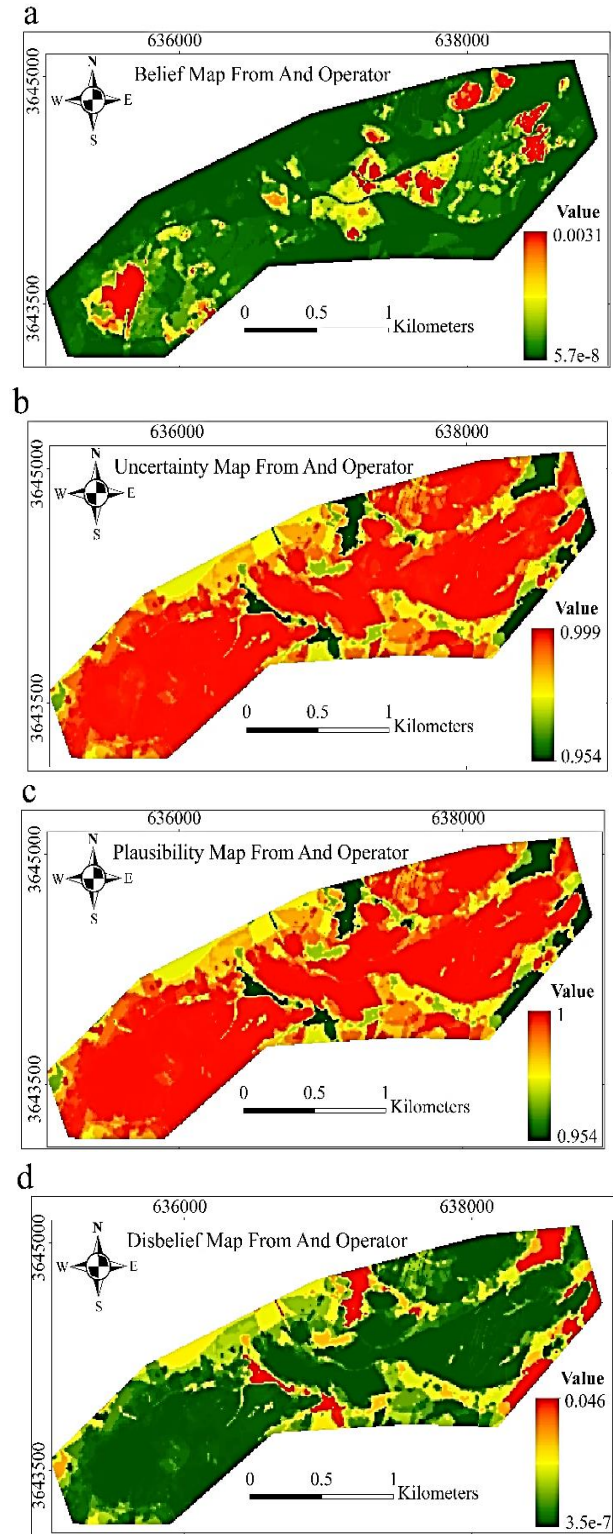

Figure 11. Maps obtained from the EBFs model using the And operator, (a) belief map, (b) uncertainty map, (c) plausibility map, and (d) disbelief map.
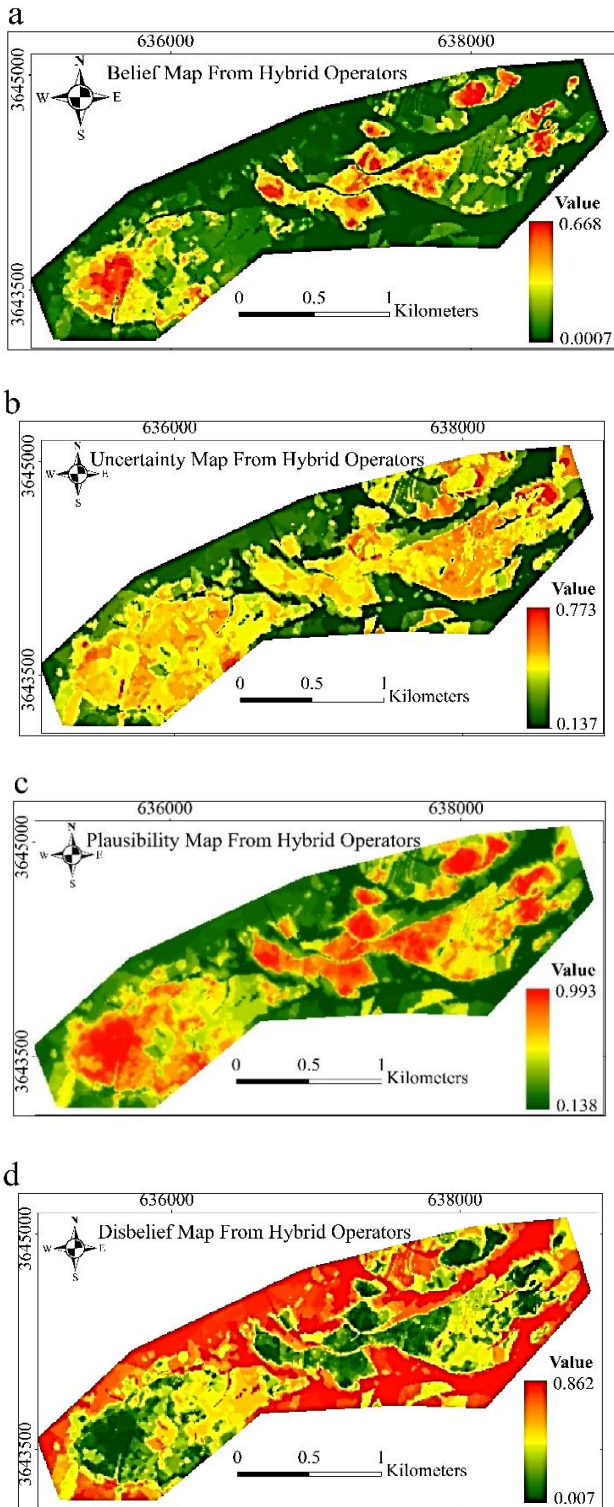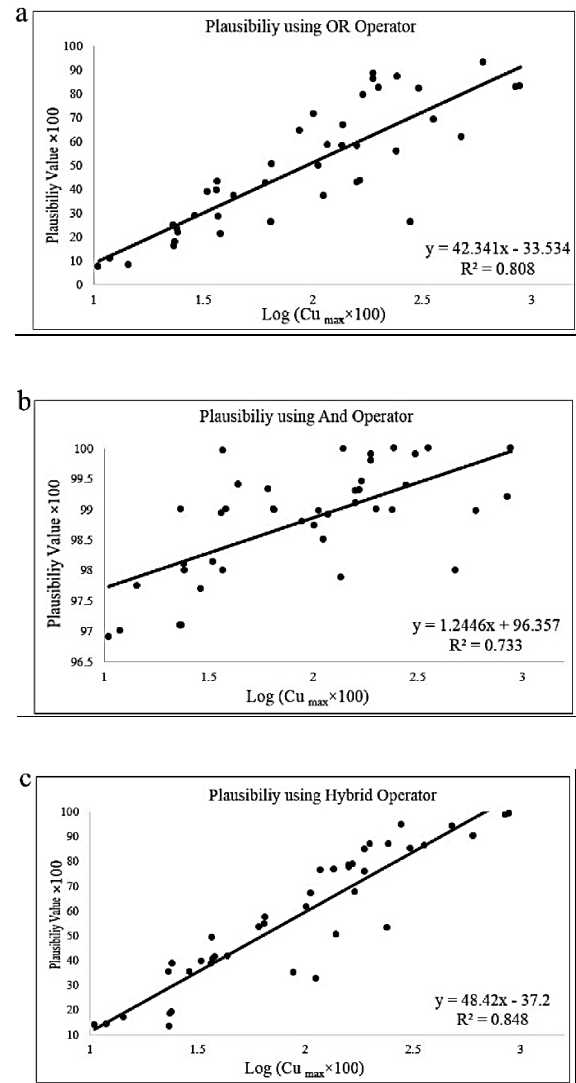
a

b

c

a

b

c

Figure 13. Scatter plot of the maximum Cu concertation versus the value of plausibility map in the location of boreholes (a) for OR operator, (b) for And operator, and (c) for hybrid operators.

d

Figure12. Maps obtained from the EBFs model using the Hybrid operators, (a) belief map, (b) uncertainty map, (c) plausibility map, and (d) disbelief map.

Table 7: Spearman's correlation coefficient of plausibility values against the Cu concentration in boreholes location.

Spearman Method	Correlation Coefficient	Pls_OR	Pls_And	Pls_Hybrid
	Cu	0.804	0.743	0.881

5. Conclusion

An exploration information system plays a crucial role in mineral prospectivity mapping using logical integration models because the evidential layers are based on the conceptual model. Various data and tools such as geochemical, geophysical, and geological data and satellite images are utilized to generate evidential layers depending on the sought target. In this research, the ASTER images were processed to extract the alterations related to the porphyry-type Cu-Mo mineralization. It was shown that different analytical techniques could be used in image processing; where among them BR, SPCA, and LS-Fit methods were selected to determine the locations of the propylitic, argillic and phyllic alterations, respectively.

High-resolution images such as Quickbird can be used to provide a tectonic layer in addition to field surveys and determine geological lineaments at the deposit scale. Automatic extraction of lineaments was performed to expedite the processing. Advanced algorithms such as the Canny algorithm and Hough transform enhance the accuracy of geological lineaments through edge detection and line extraction, respectively. The soil-geochemical method was also used to prepare geochemical layers, and magnetometry was performed to prepare the

geophysical layers. Once evidential layers are provided correctly, it is important to use appropriate integrative models and arrange and apply inferential networks to generate mineral prospectivity maps.

High-resolution images such as Quickbird can be used to provide a tectonic layer in addition to field surveys and determine geological lineaments at the deposit scale. Automatic extraction of lineaments was performed to expedite the processing. Advanced algorithms such as the Canny algorithm and Hough transform enhance the accuracy of geological lineaments through edge detection and line extraction, respectively. The soil-geochemical method was also used to prepare geochemical layers, and magnetometry was performed to prepare the geophysical layers. Once evidential layers are provided correctly, it is important to use appropriate integrative models and arrange and apply inferential networks to generate mineral prospectivity maps.

In this study, due to the importance of uncertainty in modeling, the evidential belief functions model was used because it is able to generate four maps of belief, plausibility, uncertainty, and disbelief. With the resulting four maps, we are able to better analyze the maps, data, and results. By performing three different integration models using *OR*, *And*, and Hybrid operators, it was shown that each model yielded very different results. According to the results, the hybrid model outperformed the results. The drilled boreholes were also used for validation. Based on the plausibility of binary maps, out of 25 explorative boreholes with a maximum Cu concentration over 0.5%, 21 boreholes

were located within the desired area with an area of 0.67 km² indicating the superiority of the hybrid technique in the NPCMD.

Acknowledgment

REFERENCES

[1] Bonham-Carter, G.F. (1994). Geographic Information Systems for Geoscientists Modeling with GIS, 1st ed. Pergamon, Ontario. doi: https://doi.org/10.1016/C2013-0-03864-9

[2] Cargill, S.M., & Clark, A.L. (1978). Report on the activity of IGCP Project 98. J. Int. Assoc. Math. Geol., 10, 411-417. doi: https://doi.org/10.1007/BF02461973

[3] Yousefi, M., Kreuzer, O.P., Nykänen, V., & Hronsky, J.M.A. (2019). Exploration information systems – A proposal for the future use of GIS in mineral exploration targeting. Ore Geology Reviews, 111. doi: https://doi.org/10.1016/j.oregeorev.2019.103005

[4] Kreuzer, O.P., Yousef, M., & Nykänen, V. (2020). Introduction to the special issue on spatial modeling and analysis of oreforming processes in mineral exploration targeting. Ore Geology Reviews, 119, 103391.

[5] Yousef, M., Carranza, E.J.M., Kreuzer, O.P., Nykänen, V., Hronsky, J.M.A., & Mihalasky, M.J. (2021). Data analysis methods for prospectivity modeling as applied to mineral exploration targeting: State-of-the-art and outlook. Journal of Geochemical Exploration, 229, 106839.

[6] Porwal, A., Carranza, E.J.M., & Hale, M. (2001). Extended weights-of-evidence modeling for predictive mapping of base metal deposit potential in Aravalli Province, western India. Explor. Min. Geol., 10, 273–287. doi: https://doi.org/10.2113/0100273

[7] Porwal, A., Carranza, E.J.M., & Hale, M. (2003). Artificial neural networks for mineral-potential mapping: A case study from Aravalli Province, Western India. Nat. Resour. Res., 12, 155–171. doi: https://doi.org/10.1023/A:1025171803637

[8] Oh, H.J., & Lee, S. (2010). Application of artificial neural network for gold-silver deposits potential mapping: A case study of Korea. Nat. Resour. Res., 19, 103–124. doi: https://doi.org/10.1007/s11053-010-9112-2

[9] Rahimi, H., Abedi, M., Yousefi, M., Bahroudi, A., & Elyasi, Gh.R. (2021). Supervised mineral exploration targeting and the challenges with the selection of deposit and non-deposit sites thereof. Applied Geochemistry, 128, 104940.

[10] Abedi, M., Norouzi, G.H., & Bahroudi, A. (2012). Support vector machine for multi-classification of mineral prospectivity areas. Comput. Geosci., 46, 272-283.

[11] Carranza, E.J.M., & Laborte, A.G. (2015). Random forest predictive modeling of mineral prospectivity with small number of prospects and data with missing values in Abra (Philippines). Comput. Geosci., 74, 60–70. doi: https://doi.org/10.1016/j.cageo.2014.10.004

[12] Carranza, E.J.M. (2009). Geochemical anomaly and mineral prospectivity mapping in GIS. Elsevier.

[13] Billa, M., Stein, G., Guillou-Frottier, L., Tourlière, B., Bouchot, V., Lips, A.L., & Cassard, D. (2004). Predicting gold-rich epithermal and porphyry systems in the central Andes with a continental-scale metallogenic GIS. Ore Geol. Rev., 25, 39–67.
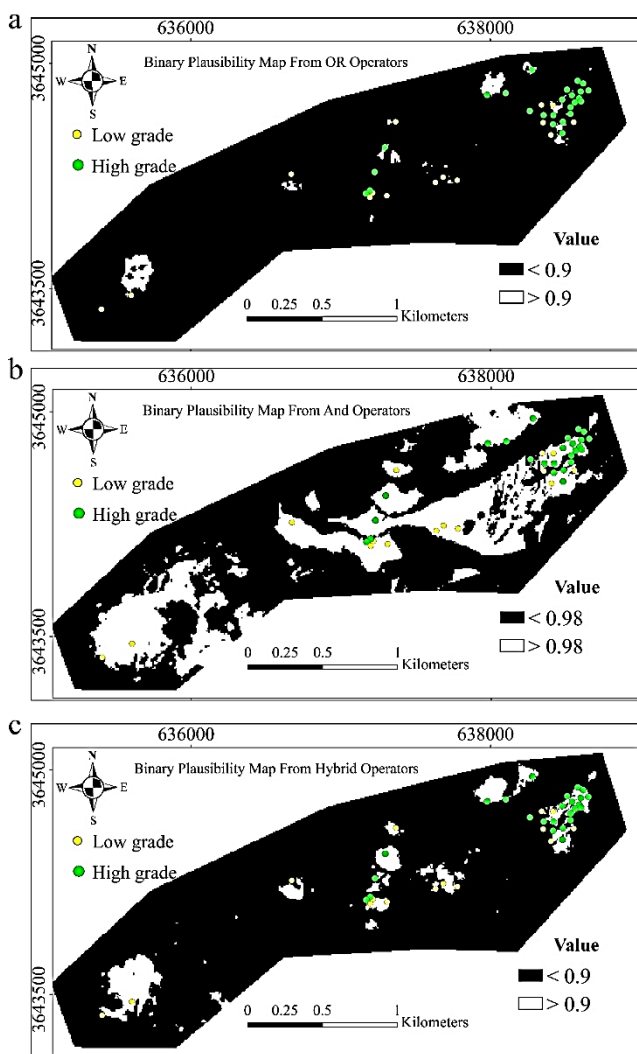
Figure 14. Binary map of plausibility and the location of boreholes in the Naysian area, (a) OR operator, (b) And operator, and (c) hybrid operators.

doi:https://doi.org/10.1016/j.oregeorev.2004.01.002

[14] Abedi, M., Norouzi, G.H., & Fathianpour, N. (2012). Fuzzy outranking approach: A knowledge-driven method for mineral prospectivity mapping. Int. J. Appl. Earth Obs. Geoinf., 21, 556–567. doi:https://doi.org/10.1016/j.jag.2012.07.012

[15] Najafi, A., Karimpour, M.H., & Ghaderi, M. (2014). Application of fuzzy AHP method to IOCG prospectivity mapping: A case study in Taherabad prospecting area, eastern Iran. Int. J. Appl. Earth Obs. Geoinf., 33, 142–154. doi:https://doi.org/10.1016/j.jag.2014.05.003

[16] Abedi, M., Torabi, S.A., & Norouzi, G.H. (2013). Application of fuzzy AHP method to integrate geophysical data in a prospect scale, a case study: Seridune copper deposit. Boll. di Geofis. Teor. ed Appl., 54, 145–164. doi:https://doi.org/10.4430/bgta0085

[17] Carranza, E.J.M. (2010). Improved wildcat modeling of mineral prospectivity. Resour. Geol., 60, 129–149. doi:https://doi.org/10.1111/j.1751-3928.2010.00121.x

[18] Carranza, E.J.M., van Ruitenbeek, F.J.A., Hecker, C., van der Meijde, M., & van der Meer, F.D. (2008). Knowledge-guided data-driven evidential belief modeling of mineral prospectivity in Cabo de Gata, SE Spain. Int. J. Appl. Earth Obs. Geoinf., 10, 374–387. doi: https://doi.org/10.1016/j.jag.2008.02.008

[19] Porwal, A., Carranza, E.J.M., & Hale, M. (2006). A hybrid fuzzy weights-of-evidence model for mineral potential mapping. Nat. Resour. Res., 15, 1–14. doi:https://doi.org/10.1007/s11053-006-9012-7

[20] Yousefi, M., & Carranza, E.J.M. (2015). Prediction-area (P-A) plot and C-A fractal analysis to classify and evaluate evidential maps for mineral prospectivity modeling. Comput. Geosci., 79, 69–81. doi: https://doi.org/10.1016/j.cageo.2015.03.007

[21] Luo, X., & Dimitrakopoulos, R. (2003). Data-driven fuzzy analysis in quantitative mineral resource assessment. Comput. Geosci. 29, 3–13. doi: https://doi.org/10.1016/S0098-3004(02)00078-X

[22] Nykänen, V., Groves, D.I., Ojala, V.J., Eilu, P., & Gardoll, S.J. (2008). Reconnaissance-scale conceptual fuzzy-logic prospectivity modeling for iron oxide copper-gold deposits in the northern Fennoscandian shield, Finland. Aust. J. Earth Sci., 55, 25–38. doi: https://doi.org/10.1080/08120090701581372

[23] Yousefi, M., & Carranza, E.J.M. (2016). Data-Driven Index Overlay and Boolean Logic Mineral Prospectivity Modeling in Greenfields Exploration. Nat. Resour. Res., 25, 3–18. doi: https://doi.org/10.1007/s11053-014-9261-9

[24] Yousefi, M., & Nykänen, V. (2017). Introduction to the special issue: GIS-based mineral potential targeting. J. African Earth Sci., 128, 1–4. doi: https://doi.org/10.1016/j.jafrearsci.2017.02.023

[25] Yousefi, M., & Nykänen, V. (2016). Data-driven logistic-based weighting of geochemical and geological evidence layers in mineral prospectivity mapping. J. Geochemical Explor., 164, 94–106. doi: https://doi.org/10.1016/j.gexplo.2015.10.008

[26] Dempster, A.P. (1968). A generalization of the Bayesian inference. J. R. Stat. Soc., 30, 205–447.

[27] Dempster, A.P. (1967). Upper and lower probabilities induced by a multivariate mapping.pdf. Ann. Math. Stat., 38, 325–339.

[28] Shafar, G. (1976). A Mathematical Theory of Evidence. Princeton University Press.

[29] An, P., Moon, W.M., & Bonham-Carter, G.F. (1994). Uncertainty management in integration of exploration data using the belief function. Nonrenewable Resour., 3, 60–71.

doi:https://doi.org/10.1007/BF02261716

[30] An, P., Moon, W.M., & Bonham-Carter, G.F. (1994). An object-oriented knowledge representation structure for exploration data integration. Nonrenewable Resour., 3, 132–145.

[31] Moon, W.M. (1990). Integration of geophysical and geological data using evidential belief function. IEEE Trans. Geosci. Remote Sens., 28, 711–720.

[32] Abedi, M., Mostafavi Kashani, S.B., Norouzi, G.H., & Yousefi, M. (2017). A deposit scale mineral prospectivity analysis: A comparison of various knowledge-driven approaches for porphyry copper targeting in Seridune, Iran. J. African Earth Sci., 128, 127–146. doi:https://doi.org/10.1016/j.jafrearsci.2016.09.028

[33] Carranza, E.J.M., & Hale, M. (2003). Evidential belief functions for data-driven geologically constrained mapping of gold potential, Baguio district, Philippines. Ore Geol. Rev. 22, 117–132. doi: https://doi.org/10.1016/S0169-1368(02)00111-7

[34] Park, N.W. (2011). Application of Dempster-Shafer theory of evidence to GIS-based landslide susceptibility analysis. Environ. Earth Sci., 62, 367–376. doi: https://doi.org/10.1007/s12665-010-0531-5

[35] Pourghasemi, H.R., & Beheshtirad, M. (2014). Assessment of a data-driven evidential belief function model and GIS for groundwater potential mapping in the Koohrang Watershed, Iran. Geocarto Int., 30, 662–685.

[36] Arab Amiri, M., Karimi, M., & Alimohammadi Sarab, A. (2015). Hydrocarbon resources potential mapping using evidential belief functions and frequency ratio approaches, southeastern Saskatchewan, Canada. Can. J. Earth Sci., 52, 182–195. doi: https://doi.org/10.1139/cjes-2013-0193

[37] Samadzadegan, F., Sharifi, M.A., Noorollahi, Y., Itoi, R., & Moghaddam, M.K. (2013). Spatial data analysis for exploration of regional-scale geothermal resources. J. Volcanol. Geotherm. Res. 266, 69–83. doi: https://doi.org/10.1016/j.jvolgeores.2013.10.003

[38] Mandelbrot, B.B. (1983). The Fractal Geometry of Nature, updated an. ed. Freeman, New York.

[39] Cheng, Q., Agterberg, F.P., & Ballantyne, S.B. (1994). The separation of geochemical anomalies from background by fractal methods. J. Geochemical Explor. 51, 109–130. doi: https://doi.org/10.1016/0375-6742(94)90013-2

[40] Afzal, P., Ahari, H.D., Omran, N.R., & Aliyari, F. (2013). Delineation of gold mineralized zones using concentration–volume fractal model in Qolqoleh gold deposit, NW Iran. Ore Geol. Rev., 55, 125–133. doi: https://doi.org/10.1016/j.oregeorev.2013.05.005

[41] Mohammadpour, M., Bahroudi, A., Abedi, M., Rahimipour, G., Jozanikohan, G., & Khalifani, F.M. (2019). Geochemical distribution mapping by combining number-size multifractal model and multiple indicator kriging. J. Geochemical Explor., 200. doi: https://doi.org/10.1016/j.gexplo.2019.01.018

[42] Zuo, R., Agterberg, F.P., Cheng, Q., & Yao, L. (2009). Fractal characterization of the spatial distribution of geological point processes. Int. J. Appl. Earth Obs. Geoinf., 11, 394–402. doi: https://doi.org/10.1016/j.jag.2009.07.001

[43] Stocklin, J. (1968). Structural History and Tectonics of Iran: A Review, American Association of Petroleum Geologists. AAPG Bulletin. American Association of Petroleum Geologists.

[44] Aghanabati, A. (2004). Geology of Iran. Geological Survey of Iran publication (In Persian), Tehran, Iran.

[45] Berberian, F., & Berberian, M. (1981). Tectono-plutonic episodes in Iran. American Geophysical Union, Washington, pp. 5–32. doi: https://doi.org/10.1029/GD003p0005

[46] McQuarrie, N., Stock, J.M., Verdel, C., & Wernicke, B.P. (2003). Cenozoic evolution of Neotethys and implications for the causes of plate motions. Geophys. Res. Lett., 30, 1-4. doi:https://doi.org/10.1029/2003GL017992

[47] Afshooni, S.Z., Mirnejad, H., Esmaeily, D., & Asadi Haroni, H.A. (2013). Mineral chemistry of hydrothermal biotite from the Kahang porphyry copper deposit (NE Isfahan), Central Province of Iran. Ore Geol. Rev., 54, 214–232. doi: https://doi.org/10.1016/j.oregeorev.2013.04.004

[48] Afzal, P., Khakzad, A., Moarefvand, P., Omran, N.R., Esfandiari, B., & Fadakar, Y. (2010). Geochemical anomaly separation by multifractal modeling in Kahang (Gor Gor) porphyry system , Central Iran. J. Geochemical Explor., 104, 34–46. doi: https://doi.org/10.1016/j.gexplo.2009.11.003

[49] Tabatabaei, S.H., & Asadi Haroni, H. (2006). Geochemical characteristics of Gor GorCu–Mo porphyry system, in: 25th Iranian Symposium on Geosciences. Geological Survey of Iran, Tehran, Iran, p. 60.

[50] Zarnab. Co, 2011. Geological and alteration studies of Kahang area. Isfahan.

[51] Sillitoe, R.H. (2010). Porphyry Copper Systems. Econ. Geol., 105, 3-41. doi: https://doi.org/10.2113/gsecongeo.105.1.3

[52] Yousefi, M. (2017). Analysis of Zoning Pattern of Geochemical Indicators for Targeting of Porphyry-Cu Mineralization: A Pixel-Based Mapping Approach. Nat. Resour. Res., 26, 429-441. doi: https://doi.org/10.1007/s11053-017-9334-7

[53] Yousefi, M. (2017). Recognition of an enhanced multi-element geochemical signature of porphyry copper deposits for vectoring into mineralized zones and delimiting exploration targets in Jiroft area, SE Iran. Ore Geol. Rev., 83, 200-214. doi: https://doi.org/10.1016/j.oregeorev.2016.12.024

[54] Abedi, M., Fournier, D., Devriese, S.G.R., & Oldenburg, D.W. (2018). Integrated inversion of airborne geophysics over a structural geological unit: A case study for delineation of a porphyry copper zone in Iran. J. Appl. Geophys., 152, 188–202. doi: https://doi.org/10.1016/j.jappgeo.2018.04.001

[55] John, D.A., Ayuso, R.A., Barton, M.D., Blakely, R.J., Bodnar, R.J., Dilles, J.H., Graybeal, F.T., Mars, J.C., McPhee, D.K., & Seal, R.R., others, (2010). Porphyry copper deposit model. Sci. Investig. Rep. 169.

[56] Cardoso-Fernandes, J., Teodoro, A.C., & Lima, A. (2018). Remote sensing data in lithium (Li) exploration: A new approach for the detection of Li-bearing pegmatites. Int. J. Appl. Earth Obs. Geoinf., 76, 10–25. doi: https://doi.org/10.1016/j.jag.2018.11.001

[57] Carrino, T.A., Crósta, A.P., Toledo, C.L.B., & Silva, A.M. (2018). Hyperspectral remote sensing applied to mineral exploration in southern Peru: A multiple data integration approach in the Chapi Chiara gold prospect. Int. J. Appl. Earth Obs. Geoinf., 64, 287–300. doi: https://doi.org/10.1016/j.jag.2017.05.004

[58] Liu, L., Feng, J., Rivard, B., Xu, X., Zhou, J., Han, L., Yang, J., & Ren, G. (2018). Mapping alteration using imagery from the Tiangong-1 hyperspectral spaceborne system: Example for the Jintanzi gold province, China. Int. J. Appl. Earth Obs. Geoinf., 64, 275–286. doi:https://doi.org/10.1016/j.jag.2017.03.013

[59] Ali, E., Abdegalil, M.Y., & Musa, A.E. (2016). Assessment of Image Ratio Technique for Gold Exploration in Arid Region Using Landsat ETM + 7 : Limitations and Possible Source of Misinterpretations, 4, 17–23. doi:https://doi.org/10.1007/BF02286438

[60] Ibrahim, O., Mamfe, V., Nsofor, C.J., Shar, J.T., Sanusi, M., & Ozigis, M.S. (2014). Mineral Detection and Mapping Using Band Ratioing and Crosta Technique in Bwari Area Council, Abuja Nigeria. Int. J. Sci. Eng. Res., 5, 1100-1108.

[61] Feizi, F., & Mansouri, E. (2014). Recognition of a porphyry system using ASTER data in Bideghan – Qom province (central of Iran). Solid Earth Discuss. 6, 1765–1798. doi: https://doi.org/10.5194/sed-6-1765-2014

[62] Honarmand, M., Ranjbar, H., & Shahabpour, J. (2012). Application of Principal Component Analysis and Spectral Angle Mapper in the Mapping of Hydrothermal Alteration in the Jebal-Barez Area, Southeastern Iran. Resour. Geol. 62, 119–139. doi: https://doi.org/10.1111/j.1751-3928.2012.00184.x

[63] Han, L., Liu, Z., Ning, Y., & Zhao, Z. (2018). Extraction and analysis of geological lineaments combining a DEM and remote sensing images from the northern Baoji loess area. Adv. Sp. Res., 62, 2480–2493. doi:https://doi.org/10.1016/j.asr.2018.07.030

[64] Masoud, A.A., & Koike, K. (2011). Auto-detection and integration of tectonically significant lineaments from SRTM DEM and remotely-sensed geophysical data. ISPRS J. Photogramm. Remote Sens., 66, 818–832. doi:https://doi.org/10.1016/j.isprsjprs.2011.08.003

[65] Rahnama, M., & Gloaguen, R. (2014). TecLines: A MATLAB-based toolbox for tectonic lineament analysis from satellite images and DEMs, part 2: Line segments linking and merging. Remote Sens., 6, 11468–11493. doi:https://doi.org/10.3390/rs61111468

[66] Mami Khalifani, F., Bahroudi, A., Aliyari, F., Abedi, M., Yousefi, M., & Mohammadpour, M. (2019). Generation of an efficient structural evidence layer for mineral exploration targeting. Journal of African Earth Sciences, Volume160, 2019,103609.

[67] Biswas, R., & Sil, J. (2012). An Improved Canny Edge Detection Algorithm Based on Type-2 Fuzzy Sets. Procedia Technol., 4, 820–824. doi: https://doi.org/10.1016/j.protcy.2012.05.134

[68] Rahnama, M., & Gloaguen, R. (2014). TecLines: A MATLAB-Based Toolbox for Tectonic Lineament Analysis from Satellite Images and DEMs, Part 1: Line Segment Detection and Extraction. Remote Sens., 6, 5938–5958. doi: https://doi.org/10.3390/rs6075938

[69] Sanjay, P.R., & Naoghare, M.M. (2015). Review on Determination of Edges by Automatic Threshold Value Generation. Int. J. Comput. Sci. Mob. Comput., 4, 58–66.

[70] Wang, Y., & Li, J. (2015). An Improved Canny Algorithm with Adaptive Threshold Selection. EDP Sci., 2015 7, 1–7.

[71] Quackenbush, L.J. (2004). A Review of Techniques for Extracting Linear Features from Imagery. Photogramm. Eng. Remote Sens., 70, 1383–1392. doi: https://doi.org/10.14358/PERS.70.12.1383

[72] Wang, J., & Howarth, P.J. (1990). Use of the Hough Transform in Automated Lineament Detection. IEEE Trans. Geosci. Remote Sens., 28, 561–567. doi: https://doi.org/10.1109/TGRS.1990.572949

[73] Mohammadpour, M., Bahroudi, A., & Abedi, M. (2020). Automatic Lineament Extraction Method in Mineral Exploration Using CANNY Algorithm and Hough Transform. Geotectonics, 54 (3), 366-382.

[74] Ajayakumar, P., Rajendran, S., & Mahadevan, T.M. (2017). Geophysical lineaments of Western Ghats and adjoining coastal

areas of central Kerala, southern India and their temporal development. Geosci. Front., 8, 1089–1104. doi: https://doi.org /10.1016/j.gsf.2016.11.005

[75] Miller, H.G., & Singh, V. (1994). Potential field tilt a new concept for location of potential field sources. J. Appl. Geophys., 32, 213–217.

[76] Saein, L.D., & Afzal, P. (2017). Correlation between Mo mineralization and faults using geostatistical and fractal modeling in porphyry deposits of Kerman Magmatic Belt, SE Iran. J. Geochemical Explor., 181, 333–343. doi:https://doi.org /10.1016/j.gexplo.2017.06.014

[77] Kavoshgaran Company Report. (2010). Soilgeochemical Explorations in Kahang Area, scale: 1:5000. Tehran, Iran.

[78] Shepard, D. (1968). A two-dimensional interpolation for irregularly-spaced data function, in: Proceedings of the 1968 ACM National Conference. pp. 517–524. doi:https://doi.org/ 10.1145/800186.810616

[79] Oskooi, B., & Abedi, M. (2015). An airborne magnetometry study across Zagros collision zone along Ahvaz–Isfahan route in Iran. Journal of Applied Geophysics, 123, 112-122.

[80] Abedi, M., & Oskooi, B. (2015). A combined magnetometry and gravity study across Zagros orogeny in Iran. Tectonophysics, 664 (28),164-175.

[81] Abedi, M., Dominique, F., Devriese, S.G.R., & Oldenburgb, D.W. (2018). Potential field signatures along the Zagros collision zone in Iran. Tectonophysics, 722 (2), 25-42.

[82] Cheng, Q. (1999). Multifractality and Spatial Statistics. Comput. Geosci., 25, 949–961. doi :https://doi.org/10.1016/S0098-3004(99) 00060-6

[83] Wang, G., Zhang, S., Yan, C., Xu, G., Ma, M., Li, K., & Feng, Y. (2012). Application of the multifractal singular value decomposition for delineating geophysical anomalies associated with molybdenum occurrences in the Luanchuan ore field (China). J. Appl. Geophys., 86, 109–119. doi:https://doi.org /10.1016/j.jappgeo.2012.07.013

[84] Wang, W., Zhao, J., & Cheng, Q. (2013). Application of singularity index mapping technique to gravity/magnetic data analysis in southeastern Yunnan mineral district, China. J. Appl. Geophys., 92, 39–49. doi:https://doi.org/10.1016/j.jappgeo.2013. 02.012.